

Remarkable heat conduction mediated by non-equilibrium phonon polaritons

<https://doi.org/10.1038/s41586-023-06598-0>

Received: 26 February 2023

Accepted: 31 August 2023

Published online: 25 October 2023

 Check for updates

Zhiliang Pan¹, Guanyu Lu¹, Xun Li², James R. McBride³, Rinkle Juneja², Mackey Long⁴, Lucas Lindsay², Joshua D. Caldwell¹ & Deyu Li¹✉

Surface waves can lead to intriguing transport phenomena. In particular, surface phonon polaritons (SPhPs), which result from coupling between infrared light and optical phonons, have been predicted to contribute to heat conduction along polar thin films and nanowires¹. However, experimental efforts so far suggest only very limited SPhP contributions^{2–5}. Through systematic measurements of thermal transport along the same 3C-SiC nanowires with and without a gold coating on the end(s) that serves to launch SPhPs, here we show that thermally excited SPhPs can substantially enhance the thermal conductivity of the uncoated portion of these wires. The extracted pre-decay SPhP thermal conductance is more than two orders of magnitude higher than the Landauer limit predicted on the basis of equilibrium Bose–Einstein distributions. We attribute the notable SPhP conductance to the efficient launching of non-equilibrium SPhPs from the gold-coated portion into the uncoated SiC nanowires, which is strongly supported by the observation that the SPhP-mediated thermal conductivity is proportional to the length of the gold coating(s). The reported discoveries open the door for modulating energy transport in solids by introducing SPhPs, which can effectively counteract the classical size effect in many technologically important films and improve the design of solid-state devices.

It has been well established that electrons and lattice vibrations (phonons) are the main energy carriers in solids^{6,7}. Therefore, discoveries of noticeable contributions to heat conduction from other energy carriers are always exciting^{8–10}. Inspired by the orders-of-magnitude enhancement of near-field radiation heat transfer between adjacent surfaces mediated by SPhPs^{11–15}, Chen et al. first predicted in 2005 that transport of SPhPs along SiO₂ thin films could enhance their thermal conductivities by several folds and identified this as the only approach to counteract the classical size effect that leads to reduced lattice thermal conductivity in thin films and other nanostructures¹. Many follow-up theoretical investigations have been reported since then^{16–19}; however, so far, experimental evidence for phonon-polariton-mediated heat conduction through thin films and nanowires is relatively scarce.

Several experimental attempts have been made in the past 5 years to explore the role of SPhPs in the thermal conductivity of thin films^{2–5}. These experiments relied on the ultralong decay length of SPhPs to distinguish their contributions from phonons and all measurements were carried out on rather long samples (>100 μm in the conduction direction). However, because of the low polariton number density, the extracted SPhP-mediated thermal conductivity is very low (<0.5 W m⁻¹ K⁻¹ at room temperature). Here we disclose how SPhPs launched by metal coatings at the end(s) of 3C-SiC nanowires enhance the wire thermal conductivity by 5.8 W m⁻¹ K⁻¹ at 300 K, which is achieved through non-equilibrium transport of SPhPs along the wire.

SPhP-mediated thermal transport

Silicon carbide nanowires were purchased from ACS Material, which are of 3C-SiC polytype, as indicated by high-resolution transmission electron microscopy; see Fig. 1a. We measured the thermal conductivity (κ) of these nanowires using a well-established micro-thermal bridge method^{20–23}, with the nanowire sample placed between two suspended membranes, which contain platinum serpentine coils serving as resistance heaters and thermometers, as shown in Fig. 1b,c. Modifications have been made to the suspended membrane so that the wire sample is placed on a 200-nm-thick SiO₂ layer on top of the platinum coil, without direct contacts with platinum electrodes. This precaution avoids launching of SPhPs into the SiC nanowire by the platinum electrodes on the suspended membranes (a scanning electron microscopy (SEM) micrograph of the more commonly used device is shown in Supplementary Fig. 4). Thermal measurements were conducted in a high-vacuum cryostat (<1 × 10⁻⁶ mbar) with no external light source involved.

In the sample preparation, we performed a wetting treatment to enhance the contact between the nanowire and the membranes²⁴. After placing each sample on the measurement device, a drop of reagent alcohol was locally delivered to each suspended membrane and evaporated at about 80 °C, which led to tight binding between the wire and the membrane. This operation reduces the wire–membrane contact thermal resistance to a negligible level, as demonstrated in Fig. 2a with overlapping thermal conductivities for the same uncoated/

¹Department of Mechanical Engineering, Vanderbilt University, Nashville, TN, USA. ²Materials Science and Technology Division, Oak Ridge National Laboratory, Oak Ridge, TN, USA. ³Vanderbilt Institute of Nanoscale Science and Engineering, Vanderbilt University, Nashville, TN, USA. ⁴Interdisciplinary Materials Science Program, Vanderbilt University, Nashville, TN, USA. ✉e-mail: deyu.li@vanderbilt.edu

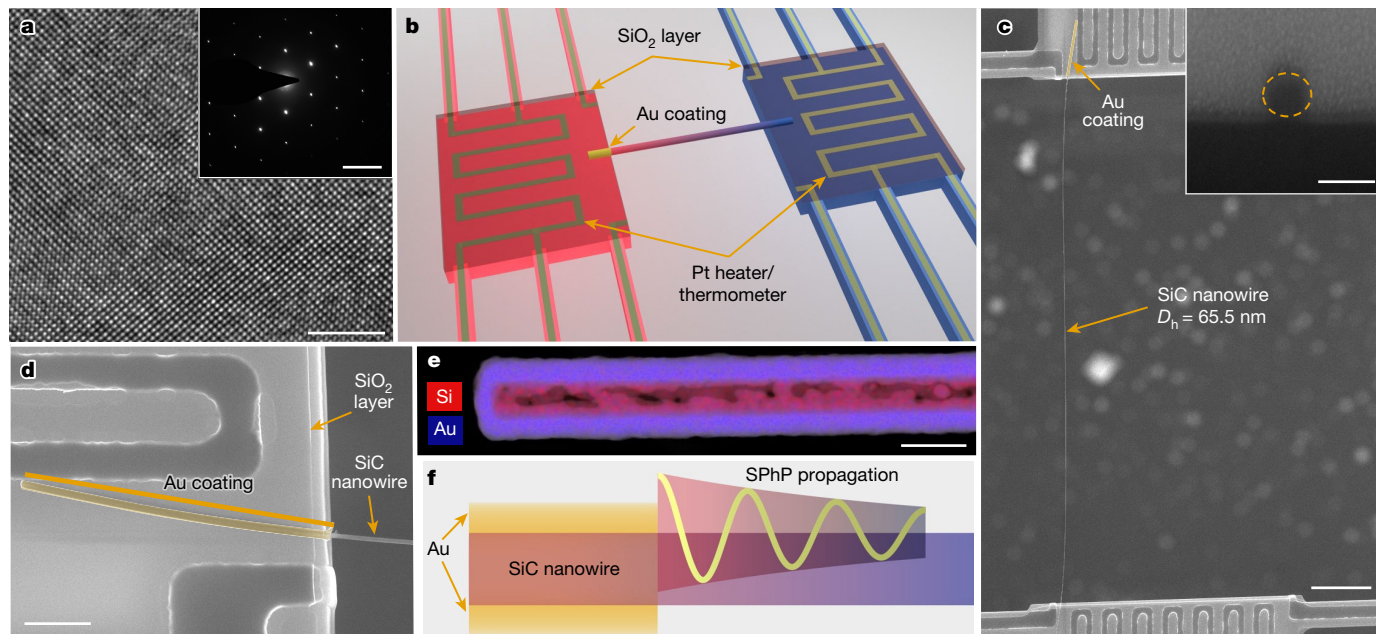


Fig. 1 | SiC nanowire sample and measurement scheme. **a**, A high-resolution transmission electron microscopy micrograph of a 65.5-nm diameter SiC nanowire (Sample S1). Inset, selected area electron diffraction pattern indicating the 3C-SiC structure. Scale bars, 5 nm, 5 nm^{-1} (inset). **b**, Schematic illustration of a SiC nanowire with Au coating on one side placed on the measurement device. **c**, An SEM micrograph of Sample S1 placed on the measurement device. Inset,

cross-section of the wire. Scale bars, $5 \mu\text{m}$, 100 nm (inset). **d**, A zoom-in SEM micrograph of the Au-coated end of the suspended membrane. For all measurements, the Au-coated portion protruded from the membrane for $<200 \text{ nm}$. Scale bar, $1 \mu\text{m}$. **e**, Element mapping of the Au-coated portion of a nanowire sample (Sample S8). Scale bar, 100 nm . **f**, Schematic illustration of SPhP propagation along nanowires.

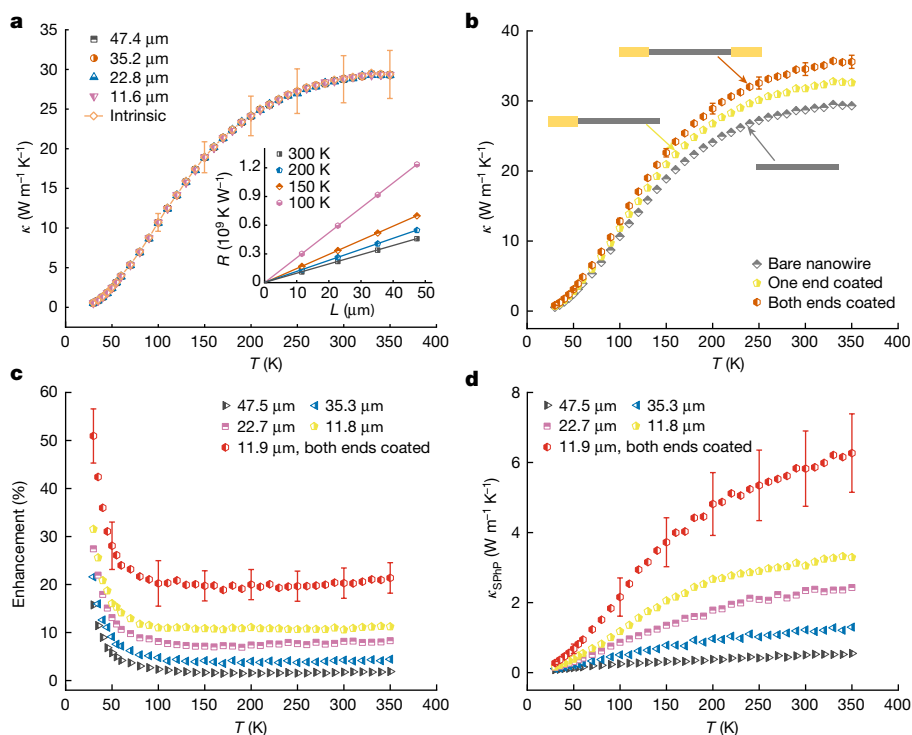


Fig. 2 | Measured thermal properties of Sample S1. **a**, Overlapping thermal conductivities of the bare wire measured with different suspended lengths and the extracted intrinsic bare-wire thermal conductivity. Inset, measured thermal resistance of the bare wire for different suspended lengths at different temperatures. **b**, Thermal conductivities of the same nanowire with and without Au coating measured with approximately the same suspended length of $11.8 \mu\text{m}$. **c**, Thermal conductivity enhancement from the Au coating for

different suspended lengths with respect to the intrinsic κ of the bare wire. **d**, Extracted SPhP thermal conductivity. For **c** and **d**, the Au coating is on one end of the nanowire unless otherwise specified. The error bars represent the standard deviations obtained according to the approach detailed in the Supplementary Information. Note that the error bars in panel **b** exclude the uncertainty from the wire cross-section, as the results are from the same wire.

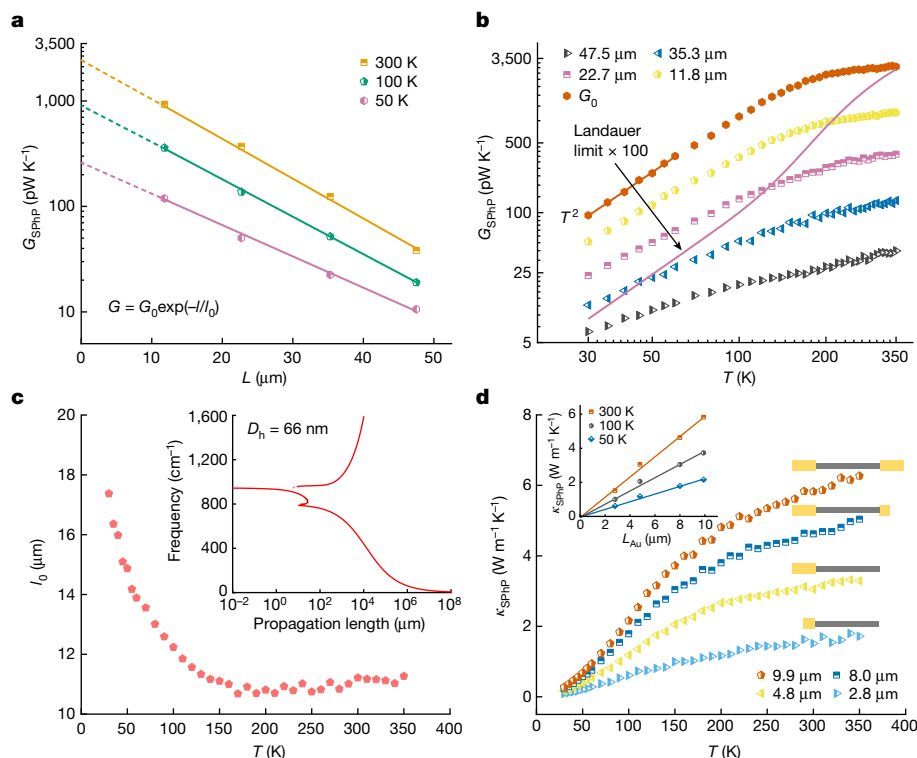


Fig. 3 | The thermal conductance of SPhPs induced by Au coating for Sample S1. a, Length dependence of G_{SPhP} . **b**, Temperature dependence of G_{SPhP} at different suspended lengths. **c**, Extracted SPhP decay lengths versus temperature, which is much smaller than predicted values, as shown in the

bare nanowire (Sample S1) with four different suspended lengths (from 11.6 μm to 47.4 μm), which was achieved by placing the wire on devices with different gap distances between the two membranes^{23,25}. The measured total thermal resistance of the wire is linear with respect to the suspended length and extrapolates to the origin (inset of Fig. 2a), further indicating the negligible contact thermal resistance.

SPhPs can be efficiently stimulated in polar thin films/nanowires with a metal film coating^{26–32} and, therefore, we wrapped one end of Sample S1 with an approximately 30-nm-thick, 4.8- μm -long Au pad (Fig. 1c,d) and remeasured κ with approximately the same four suspended lengths. The high-aspect-ratio Au pad serves as an efficient SPhP launcher and guides excited polaritons to emit from the end of the Au-coated portion into the bare SiC nanowire. As a result, Fig. 2b shows that the Au coating leads to enhanced κ in comparison with that of the same bare wire. Note that the Au-coated segment sits only on the suspended membrane and is not involved in the determination of κ for the uncoated wire segment between the membranes. Also, although surface plasmon polaritons can be stimulated in the Au coating, the undoped SiC nanowires do not support the propagation of surface plasmon polaritons. Notably, when the Au pad is on the cold side, it will still launch SPhPs, albeit at a lower average energy than the phonons on the hot side, which helps reduce the hot-side temperature and hence enhances the wire conductance (Supplementary Fig. 16).

The percentage enhancement with respect to the intrinsic κ of the same bare wire increases as the suspended length decreases (Fig. 2c). Also, the percentage enhancement becomes larger at low temperatures, by >50% for an 11.9- μm suspended length with Au coating on both ends at 30 K. Note that this suggests that, at low temperatures, it is the polariton modes outside the Reststrahlen band contributing to heat conduction, as only these low-frequency modes can be excited efficiently. The interesting length dependence indicates that SPhPs decay as they propagate along the wire, which leads to lower SPhP

inset for different SPhP frequencies for a 66-nm diameter wire. **d**, κ_{SPhP} as a function of temperature for different Au-coating lengths and as a function of Au-coating length at different temperatures (inset). Note that the legend in panel **d** refers to the total length of Au coating at the nanowire end(s).

contributions to κ for longer wires. Notably, this observation also suggests that, without the Au coating, SPhPs make negligible contributions to thermal transport, as no length dependence of κ is observed in bare nanowires. Next, we examine the net contribution of SPhPs to κ (κ_{SPhP}), which is extracted as the difference between the measured κ of the Au-coated and bare wires. As shown in Fig. 2d, κ_{SPhP} increases with temperature over the entire temperature range and the escalation rate becomes smaller as the temperature rises above 200 K.

Here we present evidence that introducing SPhPs into SiC nanowires minimally affects the lattice thermal conductivity, allowing for extraction of κ_{SPhP} as the difference between the sample with and without the Au pad. Several thermal measurements for varying lengths and coating configurations on a single nanowire are extremely challenging. As such, we obtained complete coating/length datasets (eight data points) for only four wires after numerous attempts (21 different samples measured; see Supplementary Information for further thermal data). Notably, although complete datasets from the damaged/lost samples could not be obtained, the partial results collected are fully supportive of the conclusion here.

In measurements of different samples, we found variations among the SiC nanowires in terms of how ‘lossy’ a specific wire is for SPhP propagation. This variation leads to different κ_{SPhP} . Five of the ten samples with Au coatings show κ enhancements similar to Sample S1, whereas the rest demonstrate a small enhancement that was only observable at short sample lengths. The fact that for lossy wires the κ with and without Au coatings can remain the same over a wide temperature range suggests that SPhP scattering minimally affects the phonon thermal conductivity. This is because phonon scatterings in lossy wires are dominated by the wire surface and stacking faults, which are independent of temperature, whereas the SPhP contribution to κ increases with temperature. Therefore, it is unlikely that, for lossy wires, the measured κ with the Au coating remains the same over a wide temperature range if

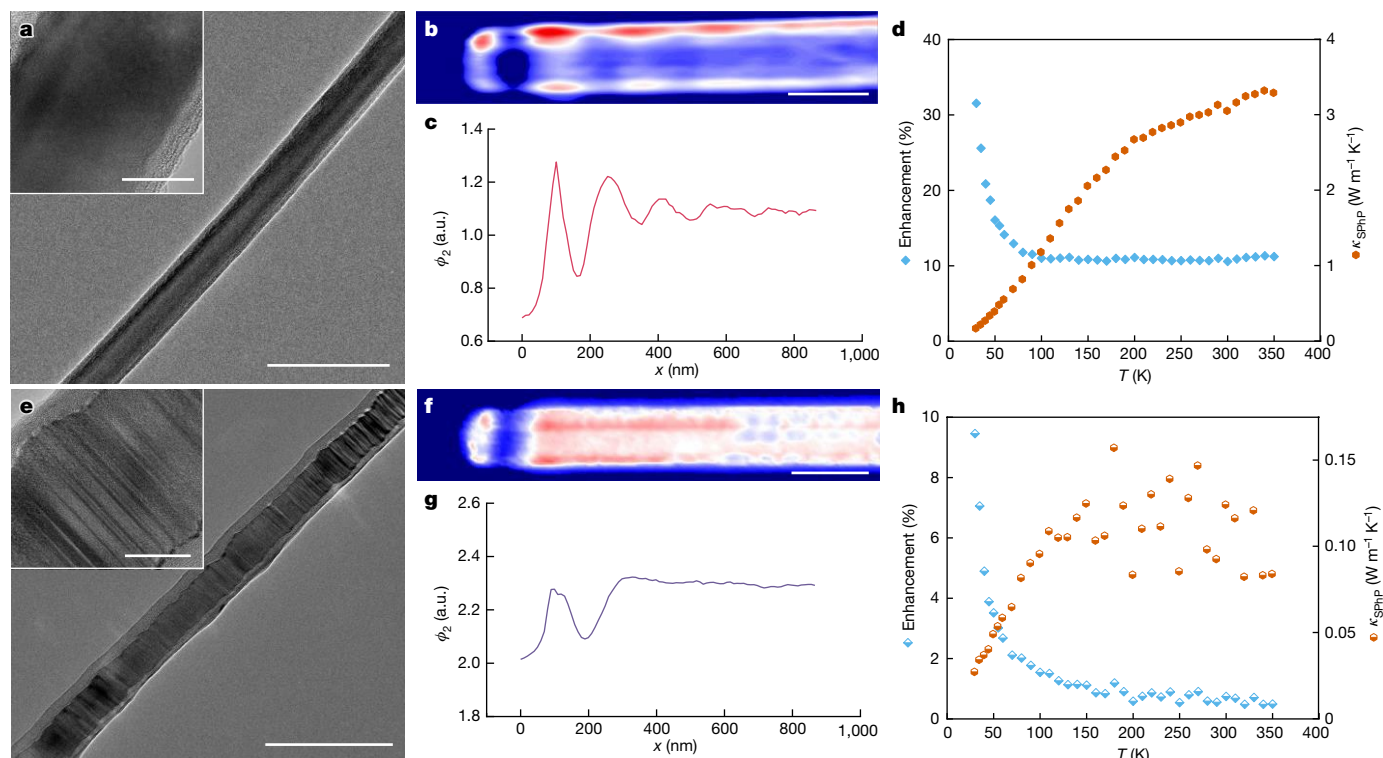


Fig. 4 | Correlation between the nanowire structure, SPHP propagation and thermal properties. **a–d**, Sample S1 (low density of stacking faults): TEM micrograph (**a**), s-SNOM mapping carried out at 865 cm^{-1} (**b**) and corresponding line profile (**c**), and κ_{SPHP} and percentage enhancement with respect to the corresponding intrinsic value (**d**). **e–h**, Sample S2 (high density

of stacking faults): TEM micrograph (**e**), s-SNOM mapping carried out at 865 cm^{-1} (**f**) and corresponding line profile (**g**), and κ_{SPHP} and percentage enhancement with respect to the corresponding intrinsic value (**h**). Scale bars, 200 nm (**a, b, e, f**), 20 nm (**a, e**, insets). Note the different scale of **h** with respect to **d**. a.u., arbitrary units.

the SPHP decay process substantially affects phonon transport. Therefore, it is reasonable to extract the difference between the measured κ with and without Au coating as κ_{SPHP} .

G_{SPHP} surpassing the Landauer limit

It is known that SPHPs decay exponentially as they propagate along polaritonic materials³³. As such, we fit the length dependence of the SPHP thermal conductance (G_{SPHP}) following the equation $G_{\text{SPHP}} = G_0 \exp(-l/l_0)$, in which G_0 and l_0 are the temperature-dependent pre-decay conductance and decay length, respectively. l represents the actual propagation length, which is equal to the suspended sample length. Indeed, the measured G_{SPHP} of the same wire with different suspended lengths demonstrates such a dependence, as shown in Fig. 3a, from which we extracted G_0 and l_0 as functions of temperature (T). Notably, G_0 demonstrates a T^2 temperature dependence below 60 K, as shown in Fig. 3b, which is consistent with the fact that SPHPs are effectively confined to the two-dimensional surface of the wire. This provides the first experimental confirmation that SPHPs in nanoscale confined systems such as nanowires are limited to two-dimensional surface transport and, therefore, the heat capacity, which is proportional to G_0 , increases with temperature following a T^2 law.

The extracted l_0 first decreases with increasing temperature ($30\text{ K} < T < \text{about } 150\text{ K}$) and then flattens as T further increases, as shown in Fig. 3c. Over the entire temperature range, l_0 is much smaller than the intrinsic propagation length expected for polaritons when using calculated phonon–phonon scattering rates for transverse optical phonons of bulk SiC to determine their attenuation (inset in Fig. 3c). Transmission electron microscopy (TEM) examinations indicate stacking faults in the SiC nanowires with varying densities among the wires. As such, we attribute the constant l_0 at elevated temperatures

to stacking-fault-induced scattering, which is independent of temperature. Below 150 K, the dominant excited-polariton wavelengths are longer and thus less sensitive to the stacking faults, which leads to an increasing decay length with decreasing T .

SPHPs exist in polar thin films and nanowires with or without the presence of a metallic coating and yet we did not observe a discernible SPHP contribution in bare wires. To further examine the effect of the Au coating, we calculated G_{SPHP} for the bare wire following the literature^{4,17}

$$G_{\text{SPHP}} = \int_0^\infty \hbar \omega \frac{\partial f_\omega(T)}{\partial T} v_\omega \tau_\omega D_\omega d\omega, \quad (1)$$

in which \hbar is the reduced Planck constant, ω is the SPHP frequency, f_ω is the equilibrium Bose–Einstein distribution, v_ω is the group velocity, τ_ω is the frequency-dependent transmission coefficient that ranges from zero to unity and $D_\omega = k_R / (2\pi v_\omega)$ is the two-dimensional density of states, with k_R being the wavevector. Setting τ_ω to unity corresponds to the Landauer limit under thermal equilibrium conditions. Notably, the calculated Landauer limit is >100 times lower than the experimentally derived G_0 over the entire measurement temperature range (Fig. 3b). This result explains why the SPHP effect on the κ of bare wires is negligible. Even for the shortest bare wire measured, the SPHP contribution to κ is less than 0.1%, which is within measurement uncertainty.

Notably, the much higher experimentally derived G_0 indicates that the Au coating efficiently couples infrared radiation into the wire. Such coupling drives the system out of thermal equilibrium, with SPHPs emitting from the Au-coated portion into the uncoated portion and leading to a two to three orders of magnitude higher number density than that determined on the basis of the local thermal equilibrium of the uncoated wire segment. To understand this unexpected finding, we consider the role of the Au pad wrapping the entire circumference

of the nanowire. It has been shown that coherent SPhPs can be excited thermally and propagate along SiC surfaces³⁴. Also, studies of nanowire lasers have suggested that nanowires can serve effectively as a waveguide³⁵. As such, we expect that polariton excitations along the entire interface between the Au pad and the SiC nanowire can be guided to emit from the end of the Au-coated portion into the uncoated wire segment. An analogy of this is to regard the entire interfacial area between the Au and the SiC wire as the surface of a parabolic reflection mirror, which guides optical modes to a smaller area on the focal plane to achieve a much higher number density.

A direct consequence of this hypothesis is that, if the suspended wire length is kept constant, κ_{SPhP} will be proportional to the length of the Au coating (L_{Au}), as long as the Au coating on each side of the nanowire is much shorter than the SPhP decay length. Note that launching and transport of SPhPs in a ballistic regime allows them to be out of thermal equilibrium with the SiC nanowire conduction channel, which leads to a G_0 well beyond the Landauer limit calculated on the basis of the equilibrium distribution function. To verify this, we varied L_{Au} of Sample S1, with the suspended nanowire length kept at roughly 11.8 μm and, indeed, κ_{SPhP} is proportional to L_{Au} , as shown in Fig. 3d. This result strongly supports the idea that the Au coating effectively guides SPhPs generated over the entire Au–SiC interface to emit into the uncoated wire segment and drives the system out of thermal equilibrium. We note that numerical simulations of the electromagnetic field distribution also support the observation that longer Au pads induce stronger electric fields and thus larger power flow, as discussed in the Supplementary Information (Supplementary Fig. 22).

Structure–property relations

The different levels of κ enhancement in different samples provide an opportunity to correlate structure and transport. As such, we conducted TEM examinations, scattering-type scanning near-field optical microscopy (s-SNOM) and thermal measurements all on each wire for two wires with different levels of SPhP contributions, as shown in Fig. 4.

Sample S1, which features a notable κ enhancement, corresponds to a low concentration of stacking faults and a long SPhP decay length derived from s-SNOM scans (Fig. 4a–d and Supplementary Fig. 17). By contrast, Sample S2 has a high density of stacking faults and features a very short SPhP decay length observed at all frequencies investigated by s-SNOM (Fig. 4e–h and Supplementary Fig. 19). Note that the s-SNOM scans are done with wires placed on top of a 300-nm-thick SiO_2 film, which leads to markedly shorter propagation lengths for both samples than for free-standing wires. This correspondence among structure, SPhP propagation and thermal properties strongly supports that the observed κ enhancement is indeed because of the transport of SPhPs in the SiC nanowires. Notably, we have also observed that the measured thermal conductance is the same as the background conductance if the uncoated wire segment between the two membranes is removed, and even the Au-coated portion remains on the membrane (see Extended Data Fig. 2). These results rule out the possibility of other effects induced by the Au coating, such as near-field³⁶ or super-Planckian radiation³⁷.

Tuning thermal conductivity using SPhPs

We note that, although at 300 K we only demonstrate approximately 21.4% κ enhancement for SiC nanowires with a total of 10- μm -long Au coatings on both ends, this relative change is with respect to a rather high baseline value of nearly 30 $\text{W m}^{-1} \text{K}^{-1}$. The highest κ_{SPhP} achieved here at 300 K is 5.8 $\text{W m}^{-1} \text{K}^{-1}$, which is more than three times that of phonon-mediated thermal conductivities for amorphous dielectric materials, including SiN_x and SiO_2 films, which are widely used in the semiconductor industry and regarded as bottlenecks in device thermal management. Because SPhPs are also suggested to exist in these films^{1–5},

purposely introducing SPhPs into microelectronic devices with metal launchers represents a promising approach to manage heat flow to eliminate hotspots.

Notably, the fact that the Au coating length is still much shorter than the SPhP decay length in our measurements indicates that the SPhP contribution has not yet been saturated. Also, the high G_0 also suggests that κ_{SPhP} beyond 5.8 $\text{W m}^{-1} \text{K}^{-1}$ can be achieved for shorter wire lengths. Overall, this discovery of SPhP-mediated non-equilibrium heat conduction driven by metallic coatings opens the door for manipulating thermal transport using SPhPs.

Online content

Any methods, additional references, Nature Portfolio reporting summaries, source data, extended data, supplementary information, acknowledgements, peer review information; details of author contributions and competing interests; and statements of data and code availability are available at <https://doi.org/10.1038/s41586-023-06598-0>.

- Chen, D., Narayanaswamy, A. & Chen, G. Surface phonon-polariton mediated thermal conductivity enhancement of amorphous thin films. *Phys. Rev. B* **72**, 155435 (2005).
- Tranchant, L. et al. Two-dimensional phonon polariton heat transport. *Nano Lett.* **19**, 6924–6930 (2019).
- Shin, S., Elzouka, M., Prasher, R. & Chen, R. Far-field coherent thermal emission from polaritonic resonance in individual anisotropic nanoribbons. *Nat. Commun.* **10**, 1377 (2019).
- Wu, Y. et al. Enhanced thermal conduction by surface phonon-polaritons. *Sci. Adv.* **6**, eabb4461 (2020).
- Wu, Y. et al. Observation of heat transport mediated by the propagation distance of surface phonon-polaritons over hundreds of micrometers. *Appl. Phys. Lett.* **121**, 112203 (2022).
- Ziman, J. M. *Electrons and Phonons: The Theory of Transport Phenomena in Solids* (Oxford Univ. Press, 2001).
- Qian, X., Zhou, J. & Chen, G. Phonon-engineered extreme thermal conductivity materials. *Nat. Mater.* **20**, 1188–1202 (2021).
- Onose, Y. et al. Observation of the magnon Hall effect. *Science* **329**, 297–299 (2010).
- Chen, X. et al. Synthesis and magnon thermal transport properties of spin ladder $\text{Sr}_4\text{Cu}_2\text{O}_4$ microstructures. *Adv. Funct. Mater.* **30**, 2001637 (2020).
- Czajka, P. et al. Planar thermal Hall effect of topological bosons in the Kitaev magnet $\alpha\text{-RuCl}_3$. *Nat. Mater.* **22**, 36–41 (2023).
- Carminati, R. & Greffet, J. Near-field effects in spatial coherence of thermal sources. *Phys. Rev. Lett.* **82**, 1660 (1999).
- Mulet, J., Joulain, K. & Carminati, R. Nanoscale radiative heat transfer between a small particle and a plane surface. *Appl. Phys. Lett.* **78**, 2931–2933 (2001).
- Shen, S., Narayanaswamy, A. & Chen, G. Surface phonon polaritons mediated energy transfer between nanoscale gaps. *Nano Lett.* **9**, 2909–2913 (2009).
- Kim, K. et al. Radiative heat transfer in the extreme near field. *Nature* **528**, 387–391 (2015).
- St-Gelais, R., Zhu, L., Fan, S. & Lipson, M. Near-field radiative heat transfer between parallel structures in the deep subwavelength regime. *Nat. Nanotechnol.* **11**, 515–519 (2016).
- Ordonez-Miranda, J. et al. Anomalous thermal conductivity by surface phonon-polaritons of polar nano thin films due to their asymmetric surrounding media. *J. Appl. Phys.* **113**, 084311 (2013).
- Ordonez-Miranda, J. et al. Quantized thermal conductance of nanowires at room temperature due to Zenneck surface-phonon polaritons. *Phys. Rev. Lett.* **112**, 055901 (2014).
- Ordonez-Miranda, J. et al. Thermal energy transport in a surface phonon-polariton crystal. *Phys. Rev. B* **93**, 035428 (2016).
- Yun, K. H., Lee, B. J. & Lee, S. H. Modeling effective thermal conductivity enhanced by surface waves using the Boltzmann transport equation. *Sci. Rep.* **12**, 15477 (2022).
- Shi, L. et al. Measuring thermal and thermoelectric properties of one-dimensional nanostructures using a microfabricated device. *J. Heat Transf.* **125**, 881–888 (2003).
- Wingert, M. C., Chen, Z., Kwon, S., Xiang, J. & Chen, R. Ultra-sensitive thermal conductance measurement of one-dimensional nanostructures enhanced by differential bridge. *Rev. Sci. Instrum.* **83**, 024901 (2012).
- Yang, L. et al. Thermal conductivity of individual silicon nanoribbons. *Nanoscale* **8**, 17895–17901 (2016).
- Yang, L. et al. Observation of superdiffusive phonon transport in aligned atomic chains. *Nat. Nanotechnol.* **16**, 764–768 (2021).
- Zhao, Y. et al. Electrical and thermal transport through silver nanowires and their contacts: effects of elastic stiffening. *Nano Lett.* **20**, 7389–7396 (2020).
- Yang, J. et al. Measurement of the intrinsic thermal conductivity of a multiwalled carbon nanotube and its contact thermal resistance with the substrate. *Small* **7**, 2334–2340 (2011).
- Dai, S. et al. Efficiency of launching highly confined polaritons by infrared light incident on a hyperbolic material. *Nano Lett.* **17**, 5285–5290 (2017).
- Chen, M. et al. Configurable phonon polaritons in twisted $\alpha\text{-MoO}_3$. *Nat. Mater.* **19**, 1307–1311 (2020).
- Novotny, L. & Hecht, B. *Principles of Nano-Optics* 2nd edn (Cambridge Univ. Press, 2012).

29. Hu, G., Shen, J., Qiu, C., Alù, A. & Dai, S. Phonon polaritons and hyperbolic response in van der Waals materials. *Adv. Opt. Mater.* **8**, 1901393 (2020).
30. Hillenbrand, R., Taubner, T. & Keilmann, F. Phonon-enhanced light–matter interaction at the nanometre scale. *Nature* **418**, 159–162 (2002).
31. Schuller, J. A., Taubner, T. & Brongersma, M. L. Optical antenna thermal emitters. *Nat. Photonics* **3**, 658–661 (2009).
32. Huber, A. J., Deutsch, B., Novotny, L. & Hillenbrand, R. Focusing of surface phonon polaritons. *Appl. Phys. Lett.* **92**, 203104 (2008).
33. Low, T. et al. Polaritons in layered two-dimensional materials. *Nat. Mater.* **16**, 182–194 (2017).
34. Greffet, J. J. et al. Coherent emission of light by thermal sources. *Nature* **416**, 61–64 (2002).
35. Eaton, S. W., Fu, A., Wong, A. B., Ning, C. Z. & Yang, P. Semiconductor nanowire lasers. *Nat. Rev. Mater.* **1**, 16028 (2016).
36. Domoto, G. A., Boehm, R. F. & Tien, C. L. Experimental investigation of radiative transfer between metallic surfaces at cryogenic temperatures. *J. Heat Transf.* **3**, 412–416 (1970).
37. Thompson, D. et al. Hundred-fold enhancement in far-field radiative heat transfer over the blackbody limit. *Nature* **561**, 216–221 (2018).

Publisher's note Springer Nature remains neutral with regard to jurisdictional claims in published maps and institutional affiliations.

Springer Nature or its licensor (e.g. a society or other partner) holds exclusive rights to this article under a publishing agreement with the author(s) or other rightsholder(s); author self-archiving of the accepted manuscript version of this article is solely governed by the terms of such publishing agreement and applicable law.

© The Author(s), under exclusive licence to Springer Nature Limited 2023

Methods

Materials

The 3C-SiC nanowires used in this study are commercially available from ACS Material (SKU NWSCO101). Synthesized using chemical vapour deposition, the wire dimension varies from 50 to 600 nm in diameter and 50 to 100 μm in length. TEM examinations indicate variations in the wire quality with different levels of stacking faults, as shown in Fig. 4. The wires came in powder form and were dispersed in reagent alcohol by sonication and then drop-casted onto the surface of a piece of polydimethylsiloxane for further manipulations.

Thermal transport measurement

Thermal conductance measurements of all SiC nanowires were performed in a cryostat (Janis CCS-400/204) under high vacuum ($<1 \times 10^{-6}$ mbar). Dual radiation shields with the inner one mounted directly on the sample holder were used to minimize the effects of radiation on the heat conduction measurements. The measurements were performed following a well-established procedure with a Wheatstone bridge configuration at the sensing side of the device to improve measurement sensitivity²¹, allowing for a resolution of about 50 pW K⁻¹ at room temperature based on the selected instrument settings for measurements in this study. The background thermal conductance for blank devices with different gap distances between the two suspended membranes were measured and deducted from the measured total thermal conductance of the nanowire samples.

Electron microscopy

SEM examinations were performed with either a Zeiss Merlin scanning electron microscope with a GEMINI II column or the integrated scanning electron microscope in a FEI Helios NanoLab G3 CX Dual Beam FIB-SEM. TEM examinations were done using an FEI Tecnai G2 Osiris S/TEM. The cross-section of the wire was obtained by first depositing a Pt/C coating using electron-beam-induced deposition as a protection layer and then cutting at different locations with a focused ion beam, following a procedure as detailed in previous reports^{24,38}. The cross-section of some samples deviates slightly from a perfect circle and we adopted the hydraulic diameter to characterize the sample size.

s-SNOM nanoimaging

For nanoimaging and nanospectroscopy of polaritonic properties in the 3C-SiC nanowires, we used a commercial s-SNOM setup from Neaspec GmbH. Sample nanowires were placed on a 300-nm SiO₂ layer on top of a silicon substrate. A conventional metal-coated (Pt-coated) AFM tip from Nanoworld was used for all the measurements. The tip tapping frequency was set to about 270 kHz and the tip tapping amplitude was set to about 60 nm for the near-field characterizations.

For the nanoimaging (s-SNOM mapping) of individual 3C-SiC nanowires on the substrate, the sample was illuminated by a *p*-polarized Quantum Cascade Laser (QCL) from Daylight Solutions. We recorded the images at different QCL frequencies with an integration time of 20 ms per pixel and a pixel size of 10 nm. The near-field signal recorded from a liquid-nitrogen-cooled HgCdTe (MCT) detector was demodulated to frequencies of 2 Ω and above. Pseudo-heterodyne interferometric detection was used to extract both the amplitude and phase channels of the near-field signals. In this work, phase channel was reported as better optical contrast was showing in the phase channel, which agrees with recent work on s-SNOM mappings of Si superlattices nanowire³⁹.

Density functional theory calculations

We performed density functional theory calculations for the optimized structure and interatomic force constants (IFCs) of bulk 3C-SiC. The

projector augmented wave method⁴⁰ was used as implemented in the Vienna Ab initio Simulation Package (VASP⁴¹⁻⁴³). The generalized gradient approximation, parameterized in ref. 44, was used for exchange correlations. The plane-wave energy cutoff was 500 eV and the energy convergence criteria was 10^{-8} eV. Ionic relaxations were performed until Hellmann Feynman forces converged to 10^{-6} eV \AA^{-1} . The structure was optimized with a Gamma-point-centred $18 \times 18 \times 18$ wavevector integration mesh.

Harmonic IFCs were calculated using the phonopy package⁴⁵ with a 432-atom $6 \times 6 \times 6$ supercell and Gamma-point-centred $3 \times 3 \times 3$ wavevector integration mesh. The anharmonic IFCs were calculated by the finite displacement method using the thirdorder.py package⁴⁶. A 250-atom $5 \times 5 \times 5$ supercell, a Gamma-point-centred $3 \times 3 \times 3$ wavevector integration mesh and a cutoff distance up to fifth nearest neighbours were used. All other calculation parameters are the same as those used for structural calculations.

Phonon dispersion and scattering rates

The calculated phonon dispersion of bulk 3C-SiC along high-symmetry directions is shown in Supplementary Fig. 1a and compared with previous measurements^{47,48}. Anharmonic phonon-phonon scattering rates were calculated from quantum perturbation theory⁴⁹⁻⁵¹

$$\Gamma_{123}^{\pm}(T) = \frac{\hbar\pi}{4N_{\text{uc}}} \frac{(f_{\omega_1}(T) + 1)(f_{\omega_2}(T) + 1/2 \pm 1/2)f_{\omega_3}(T)}{\omega_1\omega_2\omega_3} \left| V_{1,\pm 2,-3}^{(3)} \right|^2 \delta(\omega_1 \pm \omega_2 - \omega_3), \quad (2)$$

in which subscript numbers represent different phonon modes with frequency ω , the Dirac delta function δ ensures energy conservation, N_{uc} is the number of unit cells, $V_{1,\pm 2,-3}^{(3)}$ are three-phonon scattering matrix elements derived from calculated anharmonic IFCs⁵¹, $f_{\omega}(T)$ is the equilibrium Bose-Einstein distribution and \pm represent separate coalescence (+) and decay (-) processes⁶. The total scattering rate for each mode is the summation over all scattering processes that conserve energy and crystal momentum

$$\Gamma_1(T) = \frac{1}{N} \left(\sum_{2,3} \Gamma_{123}^+(T) + \frac{1}{2} \sum_{2,3} \Gamma_{123}^-(T) \right), \quad (3)$$

in which N is the number of wavevectors sampled in reciprocal space. The scattering rates as a function of temperature for a transverse optical phonon mode near the Gamma point are shown in Supplementary Fig. 1b. These rates are used to estimate the attenuation of SPhPs in the next section.

SPhP dispersion and attenuation

The frequency-dependent complex wavevector, k , is calculated from the solution of electromagnetic waveguide equations with boundary conditions for nanowire geometries⁵²⁻⁵⁵

$$\frac{\varepsilon_1 I_0'(p_1 a)}{p_1 I_0(p_1 a)} = \frac{\varepsilon_2 K_0'(p_2 a)}{p_2 K_0(p_2 a)}, \quad (4)$$

in which I_0 and K_0 are the zeroth-order modified Bessel functions of the first and second kinds, respectively. The primes indicate derivatives with respect to the arguments, $p_m = \sqrt{k^2 - \varepsilon_m k_0^2}$ are radial wavevectors, ε_m is the permittivity for medium m ($m = 1, 2$), $k_0 = \omega/c$, c is the speed of light, ω is the polariton frequency and a is the nanowire radius. The complex permittivity of the nanowire is calculated by the harmonic oscillator model⁵⁶

$$\varepsilon_1(\omega) = \varepsilon_{\infty} \left(1 + \frac{\omega_L^2 - \omega_T^2}{\omega_T^2 - \omega^2 - i\Gamma\omega} \right), \quad (5)$$

Article

in which $\epsilon_\infty = 6.7$ is the high frequency permittivity for 3C-SiC (ref. 47), $\omega_L = 964.6 \text{ cm}^{-1}$ and $\omega_T = 795.8 \text{ cm}^{-1}$ are the zone-centre frequencies of longitudinal and transverse optical phonons (Supplementary Fig. 1a), respectively, and Γ is the temperature-dependent scattering rate for transverse optical phonons (Supplementary Fig. 1b), serving as a damping parameter for the SPhPs. Here $\epsilon_2 = 1$ for the surrounding air.

The complex SPhP wavevector k is determined for each frequency by numerically solving equation (4) to give the SPhP dispersion, $\omega = \omega(k_R)$, and propagation length $\Lambda_\omega = 1/(2k_I)$, in which k_R and k_I are the real and imaginary parts of k , respectively.

Higher orders ($n > 0$) of the Bessel functions in equation (4) lead to solutions for different SPhP branch dispersions. However, these have dispersions close to the light line of the surrounding medium (that is, k_0) for the range of radii considered here (see Extended Data Fig. 1), which suggests that they can only propagate at the interface between SiC and free space. In our measurements, however, the SPhPs are launched at the interface between Au and SiC and must first propagate along the Au-coated SiC to contribute to thermal transport of the uncoated wire segment. Thus, it is reasonable to assume that only SPhPs of the $n = 0$ branch, which is under the light line of SiC (and thus confined to it), need to be considered. Calculation details and related discussions on radius-dependent and branch-dependent waveguide equations for SPhP dispersions and attenuations are provided in the Supplementary Information.

Theoretical thermal conductance of SPhPs

The thermal conductance along a nanowire at ambient temperature (T) is calculated as^{17,57}

$$G_{\text{SPhP}} = \int_0^\infty \hbar \omega \frac{\partial f_\omega(T)}{\partial T} v_\omega \tau_\omega D_\omega d\omega, \quad (6)$$

with a small temperature difference ΔT between the hot (T_h) and cold (T_c) reservoirs, $(f_\omega(T_h) - f_\omega(T_c))/\Delta T \approx \partial f_\omega(T)/\partial T$. Here \hbar is the reduced Planck constant, v_ω is the group velocity, τ_ω is a transmission coefficient whose value depends on spectral decay length (Λ_ω) and the nanowire length (L) and $D_\omega = k_R/(2\pi v_g)$ is the two-dimensional density of states, with k_R being the wavevector. The calculated G_{SPhP} is multiplied by the nanowire circumference. Because each mode ω only contributes to the conductance if it can traverse the length of the nanowire, we set $\tau_\omega = 1$ for $\Lambda_\omega > L$ and $\tau_\omega = 0$ for $\Lambda_\omega < L$. This gives sample-length-dependent thermal conductance as shown in Supplementary Fig. 2. The upper limit represents the case $\tau_\omega = 1$ for all ω , which is the Landauer limit under thermal equilibrium conditions. The calculated thermal conductance values are more than two orders of magnitude lower than that from measurements at room temperature, suggesting that the system is driven far from equilibrium by the Au coating, as discussed in the main text.

Note

During the preparation of this manuscript, D.L. has learned that the group of Dr. Renkun Chen at UC San Diego is also preparing a manuscript on SPhP-mediated heat conduction along SiO₂ nanoribbons and has had some productive discussions with Dr. Chen.

Data availability

Source data for the main figures are provided with this paper. Source data are provided with this paper.

Code availability

Original MATLAB codes used to solve for the dispersions and attenuations of bulk (Source code 1) and SPhPs (Source code 2) in Extended Data Fig. 1 are provided with this paper.

- Zhang, Q. et al. Thermal transport in quasi-1D van der Waals crystal Ta₂Pd₃Se₈ nanowires: size and length dependence. *ACS Nano* **12**, 2634–2642 (2018).
- Teitworth, T. S. et al. Water splitting with silicon p–i–n superlattices suspended in solution. *Nature* **614**, 270–274 (2023).
- Blöchl, P. E. Projector augmented-wave method. *Phys. Rev. B* **50**, 17953 (1994).
- Kresse, G. & Furthmüller, J. Efficiency of ab-initio total energy calculations for metals and semiconductors using a plane-wave basis set. *Comput. Mater. Sci.* **6**, 15–50 (1996).
- Kresse, G. & Furthmüller, J. Efficient iterative schemes for *ab initio* total-energy calculations using a plane-wave basis set. *Phys. Rev. B* **54**, 11169 (1996).
- Kresse, G. & Joubert, D. From ultrasoft pseudopotentials to the projector augmented-wave method. *Phys. Rev. B* **59**, 1758 (1999).
- Perdew, J. P., Burke, K. & Ernzerhof, M. Generalized gradient approximation made simple. *Phys. Rev. Lett.* **77**, 3865 (1996).
- Togo, A. & Tanaka, I. First principles phonon calculations in materials science. *Scr. Mater.* **108**, 1–5 (2015).
- Li, W., Carrete, J., Katcho, N. A. & Mingo, N. ShengBTE: a solver of the Boltzmann transport equation for phonons. *Comput. Phys. Commun.* **185**, 1747–1758 (2014).
- Serrano, J., Stempffer, J. & Cardona, M. Determination of the phonon dispersion of zinc blende (3C) silicon carbide by inelastic x-ray scattering. *Appl. Phys. Lett.* **80**, 4360–4362 (2002).
- Widulle, F., Ruf, T., Buresch, O., Debernardi, A. & Cardona, M. Raman study of isotope effects and phonon eigenvectors in SiC. *Appl. Phys. Lett.* **82**, 3089 (1999).
- Fermi, E. *Nuclear Physics: A Course Given by Enrico Fermi at the University of Chicago* (Univ. Chicago Press, 1950).
- Omini, M. & Sparavigna, A. Beyond the isotropic-model approximation in the theory of thermal conductivity. *Phys. Rev. B* **53**, 9064 (1996).
- Broido, D., Ward, A. & Mingo, N. Lattice thermal conductivity of silicon from empirical interatomic potentials. *Phys. Rev. B* **72**, 014308 (2005).
- Ashley, J. C. & Emerson, L. C. Dispersion relations for non-radiative surface plasmons on cylinders. *Surf. Sci.* **41**, 615–618 (1974).
- Li, Y., Qi, R., Shi, R., Li, N. & Gao, P. Manipulation of surface phonon polaritons in SiC nanorods. *Sci. Bull.* **65**, 820–826 (2020).
- Sun, S., Chen, H., Zheng, W. & Guo, G. Dispersion relation, propagation length and mode conversion of surface plasmon polaritons in silver double-nanowire systems. *Opt. Express* **21**, 14591–14605 (2013).
- Englman, R. & Ruppin, R. Optical lattice vibrations in finite ionic crystals: III. *J. Phys. C Solid State Phys.* **1**, 1515 (1968).
- Palik, E. D. *Handbook of Optical Constants of Solids* (Academic, 1998).
- Murphy, P. & Moore, J. Coherent phonon scattering effects on thermal transport in thin semiconductor nanowires. *Phys. Rev. B* **76**, 155313 (2007).

Acknowledgements We thank A. Majumdar, G. Chen, P. Reddy, G. Walker, J. Valentine, S. Shen, L. Yang and P. Gao for helpful discussions. Z.P. and D.L. thank the financial support from the National Science Foundation (award nos. 1903645 and 2114278). G.L. acknowledges support from the Army Research Office under grants W911NF-21-1-0119 and W911NF-22-P-0029. J.D.C. would like to acknowledge support from the Office of Naval Research under grant N00014-22-1-2035. Density-functional-theory-based calculations (L.L., X.L. and R.J.) were supported by the U.S. Department of Energy, Office of Science, Basic Energy Sciences, Materials Sciences and Engineering Division. Computational resources were provided by the Compute and Data Environment for Science (CADES) at Oak Ridge National Laboratory, which is supported by the Office of Science of the U.S. Department of Energy under contract no. DE-AC05-00OR22725, and by the National Energy Research Scientific Computing Center (NERSC), which is supported by the Office of Science of the U.S. Department of Energy under contract no. DE-AC02-05CH11231.

Author contributions D.L. and Z.P. designed the thermal experiment and analysed the data. Z.P. conducted the thermal measurements and SEM characterizations. G.L. and J.D.C. performed s-SNOM measurements and CST modelling, with assistance from M.L. X.L., R.J. and L.L. performed first-principles calculations on optical phonon scattering and equilibrium thermal conductance. Z.P. and J.R.M. conducted the TEM examination. D.L., J.D.C. and L.L. directed the thermal experiments, optical experiments and theoretical calculations, respectively. D.L. and Z.P. drafted the manuscript, with input from all authors. All authors participated in the writing and discussions.

Competing interests The authors declare no competing interests.

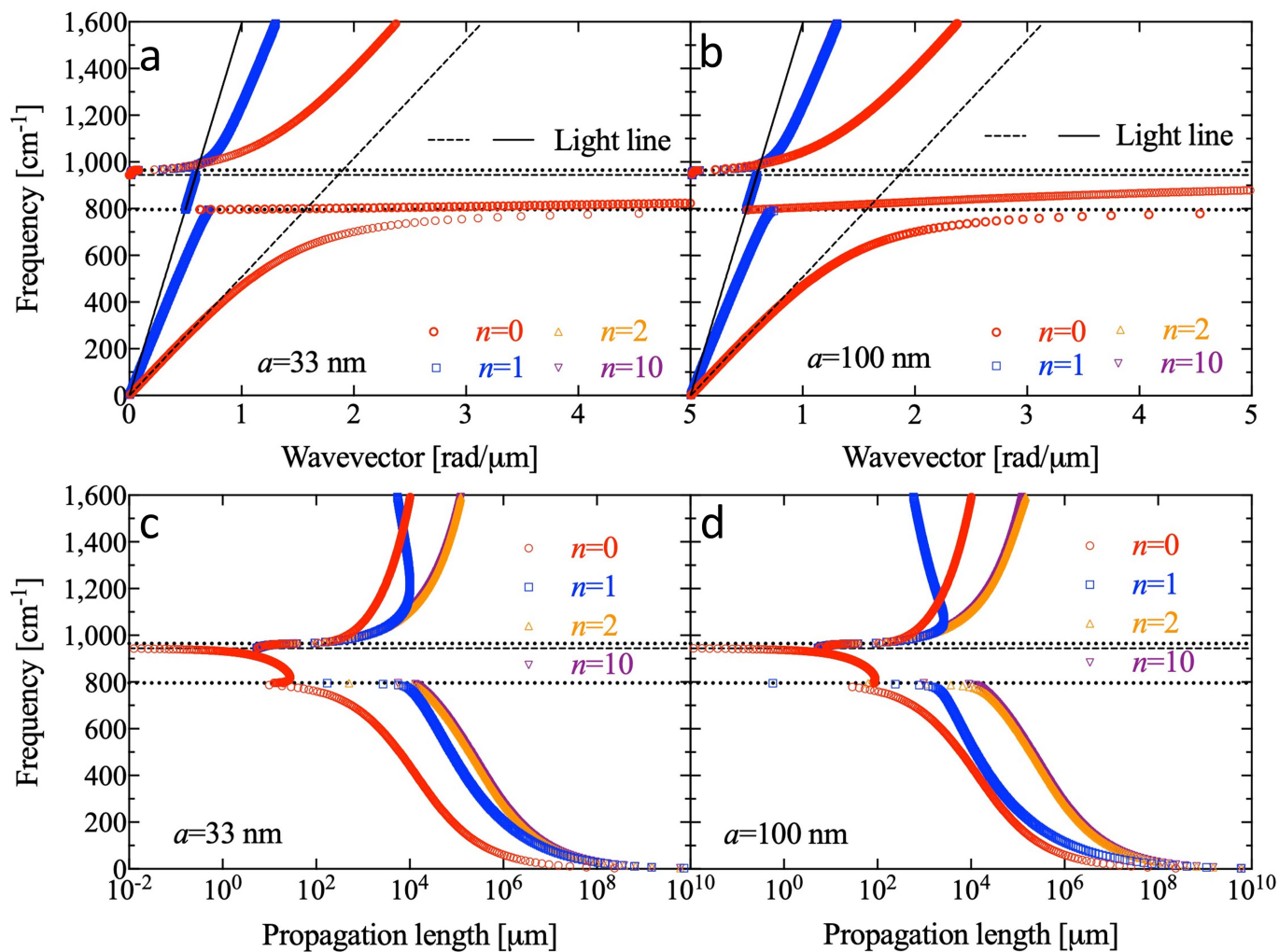
Additional information

Supplementary information The online version contains supplementary material available at <https://doi.org/10.1038/s41586-023-06598-0>.

Correspondence and requests for materials should be addressed to Deyu Li.

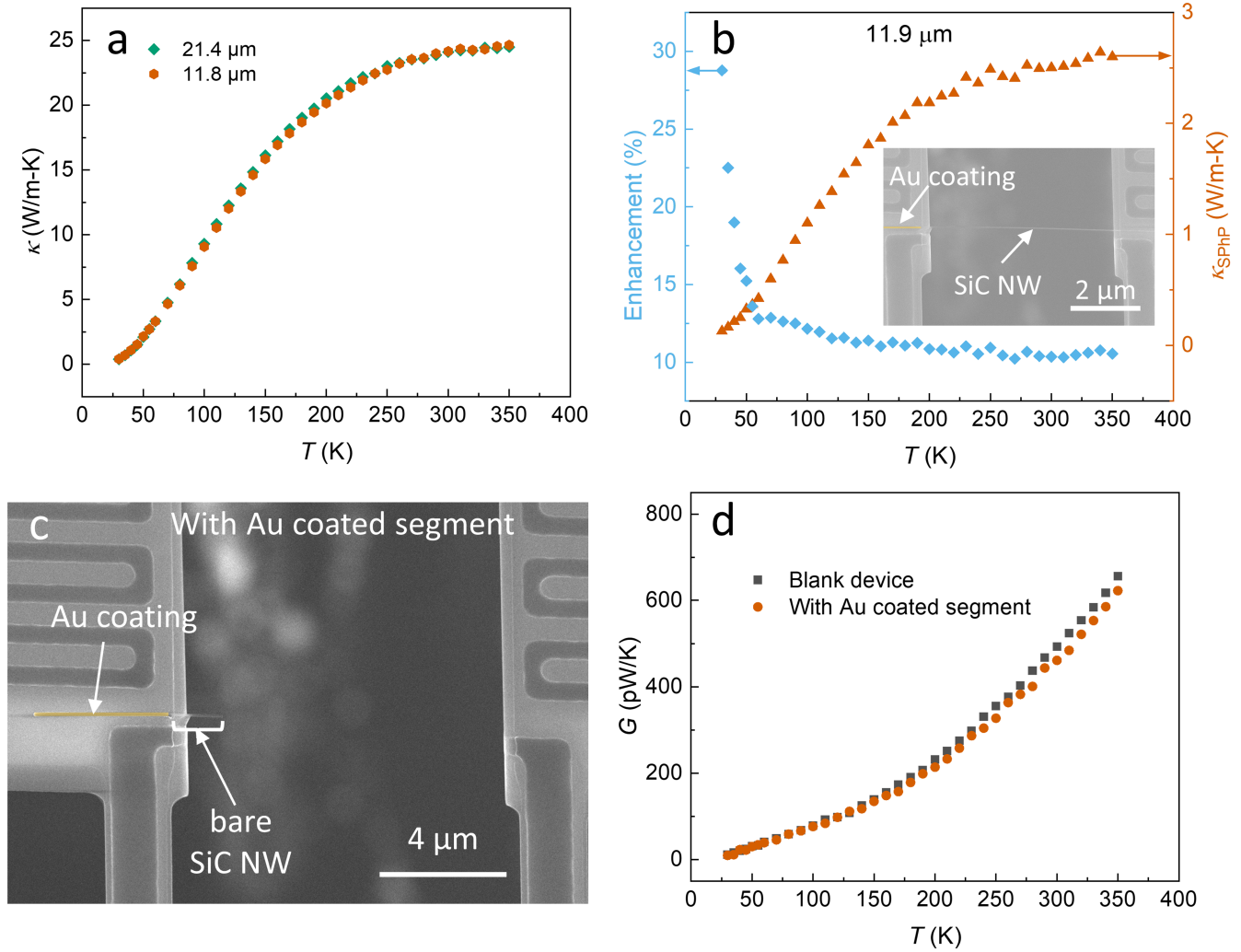
Peer review information *Nature* thanks the anonymous reviewers for their contribution to the peer review of this work. Peer reviewer reports are available.

Reprints and permissions information is available at <http://www.nature.com/reprints>.



Extended Data Fig. 1 | Theoretical calculations. Calculated SiC SPhP dispersions (a,b) and attenuations for different radii and branches (c,d). Note that all higher-order modes ($n > 1$) overlap with the first-order mode ($n = 1$) in

the upper two panels, showing the SPhP dispersion. The sloped dashed and solid lines indicate the SiC and the free-space light lines in the upper two panels, respectively.



Extended Data Fig. 2 | Further experimental data. **a**, The overlapping thermal conductivity of an uncoated SiC nanowire measured with two different suspended lengths, indicating negligible contact thermal resistance. **b**, Extracted SPHP thermal conductivity (brown symbols) and percentage enhancement (blue symbols). Inset shows the sample bridging the two

membranes, with the Au-coated segment placed on one membrane. **c**, An SEM micrograph of the sample after most of the suspended bare SiC nanowire was cut off by a sharp probe. **d**, Thermal conductance between membranes for the device with the Au-coated segment as shown in **c** (brown symbols) and a blank device of identical dimension (black symbols).